

Improved quantification of ocean carbon uptake by using machine learning to merge global models and pCO₂ data

Gloege Lucas¹, Yan Monica¹, Zheng Tian¹, and McKinley Galen A²

¹Columbia University

²Lamont Doherty Earth Observatory of Columbia University

November 16, 2022

Abstract

The ocean plays a critical role in modulating climate change by sequestering CO₂ from the atmosphere. Quantifying the CO₂ flux across the air-sea interface requires time-dependent maps of surface ocean partial pressure of CO₂ (pCO₂), which can be estimated using global ocean biogeochemical models (GOBMs) and observational-based data products. GOBMs are internally consistent, mechanistic representations of the ocean circulation and carbon cycle, and have long been the standard for making spatio-temporally resolved estimates of air-sea CO₂ fluxes. However, there are concerns about the fidelity of GOBM flux estimates. Observation-based products have the strength of being data-based, but the underlying data are sparse and require significant extrapolation to create global full-coverage flux estimates. The Lamont Doherty Earth Observatory-Hybrid Physics Data (LDEO-HPD) pCO₂ product is a new approach to estimating the temporal evolution of surface ocean pCO₂ and air-sea CO₂ exchange. LDEO-HPD uses machine learning to merge high-quality observations with state-of-the-art GOBMs. We train an eXtreme Gradient Boosting (XGB) algorithm to learn a non-linear relationship between model-data mismatch and observed predictors. GOBM fields are then corrected with the predicted model-data misfit to estimate real-world pCO₂ for 1982-2018. A benefit of this approach is that model-data misfit has reduced temporal skewness compared to the observed pCO₂ that is the target variable for other machine-learning based reconstructions. This supports a robust reconstruction by LDEO-HPD that is in better agreement with independent observations than other estimates. LDEO-HPD global ocean uptake of CO₂ is in agreement with other products and the Global Carbon Budget 2020.

1 **Improved quantification of ocean carbon uptake by**
2 **using machine learning to merge global models and**
3 **pCO₂ data**

4 **L. Gloege¹, and M. Yan², and T. Zheng^{2,3}, and G. A. McKinley⁴**

5 ¹Department of Earth and Environmental Engineering, Columbia University, New York, NY 10027, USA

6 ²Data Science Institute, Columbia University, New York, NY 10027, USA

7 ³Department of Statistics, Columbia University, New York, NY 10027, USA

8 ⁴Lamont-Doherty Earth Observatory and Department of Earth and Environmental Sciences, Columbia
9 University, New York, NY 10027, USA

10 **Key Points:**

- 11 • LDEO-HPD is in better agreement with independent data than existing products
12 • LDEO-HPD ocean uptake of CO₂ is in agreement with other products as well as
13 the Global Carbon Budget 2020 for the last decades
14 • LDEO-HPD can be used as a diagnostic tool to evaluate spatio-temporal model
15 fields

Corresponding author: Lucas Gloege, ljg2157@columbia.edu

Abstract

The ocean plays a critical role in modulating climate change by sequestering CO₂ from the atmosphere. Quantifying the CO₂ flux across the air-sea interface requires time-dependent maps of surface ocean partial pressure of CO₂ (pCO₂), which can be estimated using global ocean biogeochemical models (GOBMs) and observational-based data products. GOBMs are internally consistent, mechanistic representations of the ocean circulation and carbon cycle, and have long been the standard for making spatio-temporally resolved estimates of air-sea CO₂ fluxes. However, there are concerns about the fidelity of GOBM flux estimates. Observation-based products have the strength of being data-based, but the underlying data are sparse and require significant extrapolation to create global full-coverage flux estimates. The Lamont Doherty Earth Observatory-Hybrid Physics Data (LDEO-HPD) pCO₂ product is a new approach to estimating the temporal evolution of surface ocean pCO₂ and air-sea CO₂ exchange. LDEO-HPD uses machine learning to merge high-quality observations with state-of-the-art GOBMs. We train an eXtreme Gradient Boosting (XGB) algorithm to learn a non-linear relationship between model-data mismatch and observed predictors. GOBM fields are then corrected with the predicted model-data misfit to estimate real-world pCO₂ for 1982-2018. A benefit of this approach is that model-data misfit has reduced temporal skewness compared to the observed pCO₂ that is the target variable for other machine-learning based reconstructions. This supports a robust reconstruction by LDEO-HPD that is in better agreement with independent observations than other estimates. LDEO-HPD global ocean uptake of CO₂ is in agreement with other products and the Global Carbon Budget 2020.

Plain Language Summary

The ocean absorbs carbon from the atmosphere, which slows climate change. In order to estimate how much carbon the ocean absorbs, we need to know how much is exchanged from the atmosphere into the ocean at each location over time. The direct observations required to do this are very sparse and in some regions of the ocean, observations have never been made. One approach to fill in the gaps is to use machine-learning, which are algorithms that build a relationship for ocean carbon based on related satellite observations with global coverage. Another approach is to use computer simulations, which use mathematical equations to represent ocean processes. Here, we merge these two innovations by blending model output with machine-learning to create a hybrid product: the Lamont Doherty Earth Observatory-Hybrid Physics Data (LDEO-HPD). Particularly for the most recent decade, LDEO-HPD agrees slightly better with independent observations than other products, indicating the promise of this approach.

1 Introduction

The ocean's net uptake of CO₂ is a key component of the global carbon cycle. Quantifying how anthropogenic emissions are distributed between atmosphere, land biosphere, and ocean reservoirs with as low uncertainty as possible is needed to support international climate policy (Peters et al., 2017). The Global Carbon Budget 2020 (Friedlingstein et al., 2020) finds that for 2009-2018, the ocean sink for anthropogenic carbon was -2.5 ± 0.6 PgC/yr (negative flux into the ocean), based on global ocean biogeochemical models (GOBMs). However, four observation-based products suggest a sink that is 0.4 PgC/yr larger for this period. Do the relatively-new observation-based estimates indicate a serious problem with the long-used GOBMs? Do they require fundamental change in understanding of how carbon sinks in the ocean and on land are evolving?

Estimating the global ocean CO₂ sink requires knowledge of ocean partial pressure of CO₂ (pCO₂). The Surface Ocean CO₂ Atlas (SOCAT) is an annually compiled database of surface ocean fugacity of CO₂ (fCO₂) with over 28.2 million observations for 1957-2019 in the SOCATv2020 release (Bakker et al., 2016), mainly from volunteer observing ships.

66 fCO₂ is nearly equivalent to pCO₂, different by a 0.3% non-ideality correction; we make
67 this adjustment in our analysis to derive pCO₂ (Section 2.1). Due to limited number of
68 ships, routes, and the high cost of maintenance, the data retrieved from this observation
69 system remains sparse in space and time. Data are concentrated in the Northern Hemi-
70 sphere (Figure 1A,B,C). Using these data alone, pCO₂ cannot be quantified at all times
71 and all locations, and thus statistical extrapolations have been performed to create observation-
72 based data products (Rödenbeck et al., 2015). The carbon cycle community uses these
73 products along with global ocean biogeochemical models (GOBMs) (Friedlingstein et al.,
74 2020) to independently estimate CO₂ fluxes and, through their analysis and compari-
75 son, to improve knowledge of the global ocean carbon cycle. We propose an explicit merg-
76 ing of the strengths of both approaches in the form of a hybrid observation-based data
77 product that uses pCO₂ estimates from multiple GOBMs as a prior.

78 A GOBM is a knowledge-based model that parameterizes the physical, chemical,
79 and biological processes influencing surface ocean pCO₂ using a system of coupled dif-
80 ferential equations. GOBMs have long been taken as the best estimate of the anthro-
81 pogenic air-sea CO₂ flux, and have always been the basis for quantification of the ocean
82 carbon sink in the annual Global Carbon Budget published by the Global Carbon Project
83 since 2009 (Le Quéré et al., 2009; Friedlingstein et al., 2020). Nine GOBMs were used
84 as the basis for the Global Carbon Budget in 2019 and 2020 (Friedlingstein et al., 2019,
85 2020). These models are certainly imperfect, with substantial differences among them
86 and potentially an underestimation of CO₂ flux variability, particularly in the Southern
87 Ocean (Gruber, Landschützer, & Lovenduski, 2019; Hauck et al., 2020; Gloege et al., 2021).
88 However, based on a long history of their application to understanding and quantifica-
89 tion of air-sea CO₂ fluxes, it is a sensible to use GOBMs as a prior estimate upon which
90 data-based improvements can be made.

91 Most observation-based products find a relationship between a suite of datasets and
92 the target variable (ocean pCO₂) using machine learning algorithms. The statistical re-
93 lationships of the algorithm are dependent on the quantity and quality of SOCAT pCO₂
94 data, driver data, and the skill of the reconstruction algorithm. A recent assessment of
95 the SOM-FFN (Landschützer et al., 2014) reconstruction indicates high fidelity for the
96 mean and seasonality of pCO₂-based CO₂ flux estimates. However, pCO₂ data sparsity
97 (Figure 1A,B,C) limits the ability to reconstruct interannual to decadal timescale vari-
98 ations (Gloege et al., 2021). Though the spread across the full suite of recently-published
99 products is smaller than the spread across the current generation of models (McKinley
100 et al., 2020), there remain substantial differences in the timing and amplitude of inter-
101 annual variability (Friedlingstein et al., 2020). In a comprehensive evaluation of multi-
102 ple products, Gregor et al. (2019) find comparable skill with respect to independent data
103 in the current generation of products, and suggest that we have reached a skill limit for
104 these products that is fundamentally due to data sparsity.

105 Both GOBMs (Friedlingstein et al., 2020; Hauck et al., 2020) and observation-based
106 products (Rödenbeck et al., 2015) provide approximately global estimates of ocean pCO₂
107 and CO₂ flux. The two approaches differ significantly in the way they estimate ocean
108 pCO₂. GOBMs compute the evolution of physical and biogeochemical processes based
109 on complex systems of coupled differential equations that can only be solved numerically.
110 Observation-based products do not explicitly incorporate known physics, but instead es-
111 timate a non-linear relationship between a handful of driver datasets and ocean pCO₂
112 where these are co-located. Global full-coverage driver datasets are then processed through
113 these relationships to estimate global full-coverage pCO₂. GOBMs and observation-based
114 data products generally agree on the large-scale patterns and long-term increase in ocean
115 pCO₂ (Tjiputra et al., 2014; Landschützer et al., 2014; McKinley et al., 2016, 2020). For
116 aggregated comparisons over large regions, GOBMs have comparable root mean square
117 errors against SOCAT pCO₂ to those in the observation-based products, indicating com-
118 parable skill (Gregor et al., 2019; Hauck et al., 2020). However, GOBMs are biased high

119 when sub-sampled at SOCAT observation locations (Figure 1D). In some models, this
 120 global bias is at least partially attributable to the exclusion of the well-established wa-
 121 ter vapor correction (Dickson et al., 2007) in the calculation of atmospheric pCO₂ (McKinley
 122 et al., 2020).

123 As noted above, the pCO₂ data required to train machine learning algorithms are
 124 spatially sparse (Figure 1A,B,C). Data availability also changes over time (Figure 2A,B).
 125 This trend in data availability, combined with the long-term positive trend in ocean pCO₂
 126 ($\sim 33 \mu\text{atm}$ increase from 1980s to 2010s) has the potential to impact the ability of al-
 127 gorithms to represent the data. Machine learning, or any statistical fit, performs best
 128 when target variables distributions have the same shape as the driver variables (Goodfellow
 129 et al., 2016). With ocean pCO₂ as the target variable, the algorithm is being asked to
 130 predict a broad and right-skewed distribution (Figure 1A) that is unlike the drier vari-
 131 ables that do not have a significant temporal shift. In contrast, the difference between
 132 observed and GOBM-estimated pCO₂ has only a modest long-term trend ($\sim 9 \mu\text{atm}$ from
 133 1980s to 2010s, Figure 2C,D). Thus, if we use the difference between SOCAT observa-
 134 tions and the GOBMs as a basis for algorithm development, we largely address the afore-
 135 mentioned concern. In other words, with model-data misfit as our target variable, the
 136 skewness of the target variable is substantially reduced (Figure 2C).

137 In this study, we leverage the nine GOBMs used in the Global Carbon Budget 2020
 138 (Friedlingstein et al., 2020) and combine them with a supervised machine learning al-
 139 gorithm to create the LDEO-Hybrid Physics Data ocean pCO₂ observation-based prod-
 140 uct (LDEO-HPD). Instead of using ocean pCO₂ as the target variable, as do other data
 141 products (Landschützer et al., 2014; Rödenbeck et al., 2015; Gregor et al., 2019; Denvil-
 142 Sommer et al., 2019), the target variable for our eXtreme Gradient Boosting (XGB) al-
 143 gorithm is the misfit between SOCAT observed pCO₂ and each model where SOCAT
 144 observations exist in space and time ($\text{pCO}_{2,\text{SOCAT}} - \text{pCO}_{2,\text{GOBM}}$). Our driver data
 145 are the same suite of in situ and satellite observations used by other approaches. To make
 146 final estimates of actual ocean pCO₂, the XGB algorithm first uses full-field observed
 147 driver data to predict model misfit at all locations for each GOBM. These misfit fields
 148 are then added back to each GOBM to make the final estimate. Each GOBM is processed
 149 using a unique algorithm, and the final LDEO-HPD output is the average of the nine
 150 merged data-model estimates. See Figure 3 for a schematic. Our approach of combin-
 151 ing data-based machine learning with the physics embodied in dynamical models follows
 152 on recent innovations in physics-guided machine learning (Karpatne et al., 2017; Reich-
 153 stein et al., 2019) and the use of machine learning to correct dynamical models (Watt-
 154 Meyer et al., 2021) for earth science applications.

155 A potential additional application of the approach we develop here is to use model-
 156 data misfit fields to visualize and quantify errors in GOBM carbon cycle simulations at
 157 broader temporal and spatial scales than is currently possible with actual SOCAT data
 158 (Hauck et al., 2020). Spatio-temporal misfit mapped by the algorithm is a direct esti-
 159 mate of GOBM skill for locations where in situ data do not exist. We briefly explore this
 160 application in Section 3.1.

161 2 Methods

162 GOBM output is incorporated into a supervised machine learning algorithm to cre-
 163 ate a hybrid data product for 1982-2018. We use gradient boosting as implemented in
 164 the eXtreme Gradient Boosting (XGB) library (Chen & Guestrin, 2016). XGB learns
 165 a non-linear relationship between a suite of features and the misfit between the GOBM
 166 and direct SOCAT observations. We use this approach to upscale SOCAT pCO₂ obser-
 167 vations and create a nearly global, temporally complete data product. The upscaled pCO₂
 168 product is statistically evaluated against independent observations and other published
 169 data products. A schematic of HPD is shown in Figure 3. From pCO₂ estimated with

170 HPD, we estimate CO₂ flux using the standard bulk parameterization that relates the
 171 flux to wind speed (Wanninkhof, 1992, 2014; Fay et al., 2021).

172 2.1 Pre-processing SOCAT observations

173 We use surface ocean pCO₂ calculated from the SOCAT v2019 monthly gridded
 174 fCO₂ product. SOCAT v2019 is a quality-controlled dataset that contains observations
 175 of surface ocean fCO₂, which is converted to pCO₂ with equation 1,

$$pCO_2 = fCO_2 \cdot \exp\left(P_{atm}^{surf} \cdot \frac{B + 2\delta}{R \cdot T}\right)^{-1} \quad (1)$$

176 where P_{atm}^{surf} is the atmospheric surface pressure from ERA5, T is the sea surface tem-
 177 perature (SST) in Kelvin from National Oceanic and Atmospheric Administration (NOAA)
 178 daily optimally interpolated SST version 2 (dOISSTv2), B and δ are virial coefficients
 179 from (Weiss, 1974), R is the gas constant (Dickson et al., 2007).

180 2.2 Global Ocean Biogeochemical Models

181 As a first guess for ocean pCO₂, we use output from nine GOBMs (Table 1) which
 182 participated in the Global Carbon Budget 2020 (Friedlingstein et al., 2020), with the fi-
 183 nal year being 2018. Meteorological reanalysis and atmospheric CO₂ are used to force
 184 each model (Hauck et al., 2020). Each GOBM parameterizes the physical, chemical, and
 185 biological processes influencing surface ocean pCO₂ using a system of coupled differen-
 186 tial equations. The surface pCO₂ from each GOBM is bi-linearly interpolated from the
 187 native model grid to a 1°x1° monthly resolution to be consistent with SOCAT gridded
 188 observations (Sabine et al., 2013).

Table 1. Global Ocean Biogeochemical Models

Reference for GOBMs used in the Global Carbon Budget 2020 (Friedlingstein et al., 2020).

Global ocean biogeochemical models (GOBMs)	Reference
NEMO-PlankTOM5	Buitenhuis et al. (2013)
MICOM-HAMOCC (NorESM1-OCv1.2)	Schwinger et al. (2016)
MPIOM-HAMOCC6 (MPI)	Paulsen et al. (2017)
NEMO3.6-PISCESv2-gas (CNRM)	Berthet et al. (2019)
CISRO	Law et al. (2017)
FESCOM-1.4-REcoM2	Hauck et al. (2020)
MOM6-COBALT (princeton)	Adcroft et al. (2019)
CESCM-ETHZ	Doney et al. (2009)
NEMO-PISCES (IPSL)	Aumont et al. (2015)

189 2.3 Machine learning method and the LDEO-HPD product

190 Extreme Gradient Boosting (XGB) (Chen & Guestrin, 2016) is a supervised ma-
 191 chine learning algorithm where multiple features, X , are used to predict a target vari-
 192 able y . The XGB algorithm can then be used to estimate a function, $f(X)$, such that:
 193 $y \approx f(X)$. The algorithm begins with an initial guess for y , a choice to which the al-
 194 gorithm is not sensitive. As illustrated in Figure 3B, a decision tree is used to learn the
 195 difference between the training data and the initial guess. This new tree is added to the

196 initial guess. This process of adding trees to correct the errors made in the summation
 197 of previous trees is repeated until either a predefined number of trees has been made,
 198 or when adding an additional tree results in no further improvement. The final predic-
 199 tion is the sum of all trees such that the closest fit of input data and algorithm output
 200 is achieved. A mean-squared-error (MSE) loss function is minimized using gradient de-
 201 scent.

202 Gradient boosting algorithm, as implemented in the eXtreme Gradient Boosting
 203 (XGB) library version 0.9 with the scikit-learn wrapper (Chen & Guestrin, 2016), is used
 204 to find a non-linear relationship between a suite of input features and the misfit between
 205 each GOBM and SOCAT $p\text{CO}_2$: ($p\text{CO}_{2,\text{SOCAT}} - p\text{CO}_{2,\text{GOBM}}$). This algorithm was
 206 chosen because it leads to a better fit to input data than the other options considered,
 207 neural network or random forest (Stamell et al., 2020). To estimate $p\text{CO}_2$ at each spa-
 208 tial location, the algorithm relies on datasets with full, or approximately full, global cov-
 209 erage (Table 2): Sea Surface Temperature (SST) and Surface Chlorophyll-a (Chl-a) from
 210 satellite; Sea Surface Salinity (SSS) from a compilation of in-situ data sources; Mixed
 211 layer depth (MLD) climatology from ARGO floats; and atmospheric CO_2 mixing ratio
 212 ($x\text{CO}_2$) from station sites. These variables serve as proxies for known processes affect-
 213 ing $p\text{CO}_2$. Solubility is set by SSS and SST. Biological uptake of dissolved inorganic car-
 214 bon (DIC) is indicated by Chl-a. Biological productivity and entrainment of DIC are in-
 215 fluenced by MLDs. The long-term growth of ocean $p\text{CO}_2$ is driven by atmospheric $x\text{CO}_2$.
 216 Additional annual mean anomaly features are derived for SST and Chl-a by subtract-
 217 ing the annual mean from each year. These features help the algorithm learn more com-
 218 plex relationships and capture intra-annual variability. N-vector transformation (Gade,
 219 2010; Sasse et al., 2013; Gregor et al., 2017) of latitude and longitude is included to help
 220 the algorithm learn spatial relationships. Time transformation of the day of year con-
 221 strains seasonality (Gregor et al., 2017).

222 The features and associated $p\text{CO}_2$ misfit are split into three sets: validation, train-
 223 ing, and testing. The validation is used to optimize the algorithms hyperparameters, which
 224 defines the architecture of decision trees used in the model. The training set is used to
 225 construct the decision trees. The withheld test set is used to evaluate performance on
 226 a completely independent dataset, individual years are withheld for the test set to re-
 227 tain individual ship tracks and increase the independence of test data from training and
 228 validation data (Gregor et al., 2019).

229 Our XGB algorithm uses 1500 decision trees each with a max depth of 9 levels or
 230 until no further splits to the samples in that node are possible. Each new tree uses 95%
 231 of the features and a random subsample of observations with replacement. The weight
 232 of each sequential tree is reduced by 5%. Light L1 regularization was applied to control
 233 overfitting and loss is measured using mean-squared error (MSE).

234 XGB is used to estimate spatio-temporal estimates of the misfit for each of nine
 235 GOBMs. Misfit estimates at all locations in space and time are added back to the orig-
 236 inal GOBM to correct the GOBM toward the data. This process is repeated for each of
 237 the nine GOBMs. The final result is then the average of all nine predictions. A schematic
 238 of HPD is shown in Figure 3.

Table 2. Feature and target datasets

Summary of the products, variables, and data processing steps used for feature and target variables. Data processing is described in the text. Symbol next to each product identifies the source.

Group: product	Variable	Abbreviation	Processing
SOCATv2019*	Partial pressure of ocean CO ₂	pCO ₂	See section 2.1
NOAA:OISSTv2 [†]	Sea Surface Temperature	SST	-
	SST seasonal anomaly	SST'	SST - annual average
	Sea Ice Fraction	ICE	-
Met Office:EN4 [‡]	Sea Surface Salinity	SSS	-
NOAA:GLOBALVIEW [§]	Atmospheric CO ₂ mixing ratio	xCO ₂	-
DeBoyer:Mixed Layer Depth	Mixed Layer Depth	MLD	$\log_{10}(MLD)$
ESA:GlobColour [¶]	Chlorophyll-a	Chl a	$\log_{10}(Chla)$
	Chl a seasonal anomaly	Chl a'	chl a - annual average
-	Day of year	J_1	$\sin\left(\frac{j*2\pi}{365}\right)$
-		J_2	$\cos\left(\frac{j*2\pi}{365}\right)$
-	n-vector	A	$\sin(\lambda)$
		B	$\sin(\mu) \cos(\lambda)$
		C	$-\cos(\mu) \cos(\lambda)$

* Source: <https://www.socat.info/>

† Source: <https://www.esrl.noaa.gov/psd/data/gridded/data.noaa.oisst.v2.html>

‡ Source: <https://www.metoffice.gov.uk/hadobs/en4/>

§ Source: https://www.esrl.noaa.gov/gmd/ccgg/globalview/co2/co2_intro.html

|| Source: <http://www.ifremer.fr/cerweb/deboyer/mld/home.php>

¶ Source: <http://www.globcolour.info/>

Table 3. Validation datasets

Accuracy of pCO₂ and total number of 1° x1° grid points is shown for each dataset.

Dataset	Accuracy (μatm)	Grid points	Reference
LDEO database version 2018*	$\pm 2.5 \mu atm$	16161	Takahashi et al. (2019)
GLODAPv2 [†]	$> 12 \mu atm$ at $400 \mu atm$	5976	Gregor et al. (2019)
BATS [†]	$4 \mu atm$ at $400 \mu atm$	246	Bates (2007)
HOT [†]	$< 7.6 \mu atm$ at $400 \mu atm$	214	Dore et al. (2009)

* pCO₂ measured with pCO₂ equilibrator

† pCO₂ estimated from DIC and TA

239

2.4 Independent datasets

240

241

242

243

244

245

246

247

248

Observations not included in the SOCAT database are used to validate the method (Table 3). These datasets include the Lamont-Doherty Earth Observatory (LDEO) database, with SOCAT data removed; and GLObal Ocean Data Analysis Project version 2 (GLODAPv2). Two time series sites are also used for validation: Bermuda Atlantic Time-series Study (BATS) and Hawaii Ocean Time-series (HOT). In these datasets, pCO₂ is either directly measured or inferred from observations using carbonate system calculations with inputs of Dissolved Inorganic Carbon (DIC) and Total Alkalinity (TA). The cbsyst package (Hain et al., 2015) is used for carbonate system calculations. For decadal comparisons, timeframes are 1990s (1990-1999), 2000s (2000-2009) and 2010s (2010-2018).

249

250

251

252

253

254

255

256

257

258

259

260

The uncertainty in derived pCO₂ is dependent on the accuracy of the input measurements. For the modern ocean, cbsyst calculations are consistent with the constants of (Lueker et al., 2000), and result in a 1.9% standard deviation in pCO₂ when DIC and TA uncertainties are 2.0 and 4.0 mol kg⁻¹, respectively. For GLODAP, Bockmon and Dickson (2015) suggests an uncertainty of $5 \frac{\mu\text{mol}}{\text{kg}}$ for DIC and TA, thus suggesting an uncertainty greater than 1.9%. Gregor et al. (2019) estimate the uncertainty of GLODAP pCO₂ to be $>12 \mu\text{atm}$ at $400 \mu\text{atm}$. Although the measurements have high uncertainty, given the sparsity of the SOCAT database, including GLODAP as a validation dataset outweighs its omission, consistent with previous studies (Gregor et al., 2019; Gregor & Gruber, 2021). At BATS the uncertainty is about $4 \mu\text{atm}$ (Bates, 2007) while at HOT it is $<7.6 \mu\text{atm}$ (Dore et al., 2009). LDEO pCO₂ has uncertainty of $2.5 \mu\text{atm}$ (Takahashi et al., 2019).

261

2.5 Regression metrics

262

263

264

265

266

A suite of regression metrics are used to compare the predictions (P) to the observations (O) (Stow et al., 2009). Metrics considered include correlation (r), bias, and root mean squared error (RMSE). Multiple metrics are considered in order to provide a thorough appraisal of each method. Metrics are displayed in a Taylor diagram (Taylor, 2001).

267

268

269

270

271

272

273

274

275

276

277

Pearson correlation coefficient (r) measures the tendency of the predicted and observations to vary together, bounded between $-1 < r < 1$, with values near 1 indicating that they vary together and -1 indicating an inverse relationship. Correlation is also a measure of how well the phase is captured. Values near 1 and -1 indicate that the predictions and observations are perfectly in or out of phase, respectively. Intermediate values indicate a phase shift between the two signals, with values closer to zero indicating a larger phase shift between signals. The squared correlation r^2 , or coefficient of determination, represents the variance explained by the regression. Correlation is defined as the covariance between predictions and observations divided by the product of their standard deviations, $r = \frac{\text{cov}(P,O)}{\sigma_P \sigma_O}$, σ_P and σ_O represent the standard deviation of the predictions and observations, respectively.

278

279

280

281

282

283

284

285

286

287

288

Bias, average absolute error (AAE), and RMSE each measure the size of discrepancies, with values near zero indicating a close match between predictions and observations. However, each metric has strengths and weaknesses. Bias is simply calculated as the long-term mean difference between predictions and observations ($\text{bias} = \overline{P} - \overline{O}$), where overbars represent the temporal mean. Positive and negative bias values indicate predictions that are generally overestimated and underestimated respectively. Thus, bias provides a measure of the direction of discrepancy. However, bias values falling close to zero can be misleading with significant positive offsets at one point in space or time canceling out significant negative offsets elsewhere. $\text{RMSE} = \sqrt{(P - O)^2}$ measures of the magnitude of discrepancy, but squaring the misfit makes RMSE sensitive to outliers. Alternatively, $\text{AAE} = |P - O|$ treats each misfit equally, but is a less commonly used met-

289 ric. We report bias, AAE and RMSE since each one provides a different insight into the
290 goodness-of-fit.

291 2.6 Area coverage

292 The LDEO-HPD product covers 89.6% of the total ocean area, leaving out the Arc-
293 tic and coastal zones. Before estimating the net carbon flux from observation-based prod-
294 ucts, we use the method of (Fay et al., 2021) to fill spatial gaps in the pCO₂ product with
295 climatology (Landschützer, Laruelle, et al., 2020) plus the global-mean trend. This fills
296 in the 10.4% to create a global gap-free product. Climatological filling lowers global mean
297 pCO₂ from 356 μatm to 352 μatm in the final product. This climatological filling tech-
298 nique (Fay et al., 2021) was also applied to each observational data product to which we
299 compare our results (Table 5).

300 2.7 Air-sea CO₂ flux

301 The air-sea CO₂ exchange was calculated using a bulk parameterization (equation
302 2):

$$F_{CO_2} = k_w S_{CO_2} (1 - f_{ice}) (pCO_2^{atm-moist} - pCO_2^{ocean}) \quad (2)$$

303 which parameterizes the air-sea CO₂ flux (F_{CO_2}) as a function of the gas transfer veloc-
304 ity (k_w), CO₂ solubility (S_{CO_2}), ice fraction (f_{ice}), and partial pressure of CO₂ in moist
305 air ($pCO_2^{atm-moist}$) and surface ocean (pCO_2^{ocean}). Solubility is calculated following Weiss
306 (1974) and partial pressure of moist air ($pCO_2^{atm-moist}$) is calculated following equation
307 3,

$$pCO_2^{atm-moist} = xCO_2 (P_{atm} - pH_2O) \quad (3)$$

308 where xCO_2 is the dry air mixing ratio of atmospheric CO₂, P_{atm} is the total atmospheric
309 pressure, and pH_2O is the saturation vapor pressure (Dickson et al., 2007). We use the
310 Wanninkhof (1992) formulation for the gas transfer velocity (equation 4):

$$k_w = k_{w,scaled} u^2 \left(\frac{Sc}{660} \right)^{-0.5} \quad (4)$$

311 which parameterizes k_w as a function of wind speed squared (u^2) and the Schmidt num-
312 ber (Sc). k_w is scaled by a factor of $k_{w,scaled}$ for each wind product to match the inva-
313 sion of bomb ¹⁴C (Fay et al., 2021). Three wind products were used (Table 4). Flux was
314 calculated separately for each wind product and then averaged to create the final best
315 estimate.

316 pCO₂ measured in situ and compiled in the SOCAT database is set by the com-
317 bination of the anthropogenic and natural background carbon cycles. Thus, the calcu-
318 lated flux is the net, or contemporary, flux (F_{NET}).

Table 4. Wind speed products used to calculate CO₂ flux

Wind speed product	Reference
CCMPv2.0*	Mears et al. (2019)
ERA5 [†]	Hersbach et al. (2020)
JRA-55 [‡]	Harada et al. (2016)

* Source: <http://www.remss.com/measurements/ccmp/>

[†] Source: <https://www.ecmwf.int/en/forecasts/datasets/reanalysis-datasets/era5>

[‡] Source: <https://jra.kishou.go.jp/JRA-55/>

319

2.8 Estimating anthropogenic carbon flux from the net flux

320

321

322

323

The net CO₂ flux is the sum of an anthropogenic and a natural component ($F_{NET} = F_{NAT} + F_{ANT}$). Surface ocean pCO₂ quantifies F_{NET} , while interior ocean data quantify F_{ANT} . Closure terms are required to compare these independent quantifications of the ocean carbon sink.

324

325

326

327

328

329

330

331

332

333

334

335

336

The dominant net air-sea flux due to the natural carbon cycle is the outgassing of riverine carbon fluxed into the ocean and then slowly outgassed by the ocean (Aumont et al., 2001). The community’s estimate of the net riverine-induced carbon outgassing (F_{RIV}) is still evolving. Here we use an average of three estimates representing the spread of the available approaches: a geochemical budgeting perspective ($+0.45 \pm 0.18$ PgC/yr; Jacobson et al. (2007)), a meridional heat constraint approach ($+0.78 \pm 0.41$ PgC/yr; Resplandy et al. (2018)), and a process-based ocean model ($+0.23$ PgC/yr; Lacroix et al. (2020)). Since no uncertainty is presented for the Lacroix et al. (2020) estimate, we assume a 50% 1σ uncertainty, which is consistent with the relative magnitude of uncertainty for the other two estimates. Combining these three estimates, we derive an estimate of carbon efflux due to river input to the ocean in the observation-based product flux estimates of $+0.49 \pm 0.26$ PgC/yr. This $F_{RIV} \approx F_{NAT}$ will be removed from F_{NET} estimates from HPD and other products to arrive at F_{ANT} .

337

338

339

340

Watson et al. (2020) propose significant adjustments to SOCAT data to account for a cool and salty near-surface ocean; this adjustment would drive a large increase in F_{NET} . This remains controversial and requires more study. We do not include this adjustment.

341

342

343

344

345

346

347

348

349

350

351

352

353

Anthropogenic carbon accumulation can be estimated from interior ocean observations, for which a global survey is completed approximately once per decade, and thus this component is estimated over a defined time period. Gruber, Clement, et al. (2019) find F_{ANT} at -2.6 ± 0.3 PgC/yr for 1994-2007. A changing ocean circulation may have modified F_{NAT} over 1994-2007 through a non-steady state outgassing flux of natural carbon. Thus, a natural non-steady state flux ($F_{NAT,NS}$) has been proposed (Gruber, Clement, et al., 2019), i.e. $F_{NAT} = F_{NAT,NS} + F_{RIV}$. Applying the transient steady state assumption to F_{NET} from one observation-based product (Landschützer et al., 2016), Gruber, Clement, et al. (2019) find $F_{NAT,NS} = +0.38$ PgC/yr. However, the transient steady state assumption is known to hold when atmospheric carbon accumulation is exponential, and this has not been the case in recent decades (Raupach et al., 2014; Ridge & McKinley, 2020). This estimate of $F_{NAT,NS}$ is likely an upper bound. Nevertheless, we follow Gruber, Clement, et al. (2019) and adjust their F_{ANT} estimate by this amount.

354

355

356

357

358

359

Adjusting the F_{ANT} estimate of Gruber, Clement, et al. (2019) leads to $F_{ANT} + F_{NAT,NS} = -2.2 \pm 0.3$ PgC/yr for 1994-2007. Earlier, for the IPCC AR4, Denman et al. (2007) synthesized multiple estimates from ocean and atmosphere tracer studies to estimate $F_{ANT} = -2.2 \pm 0.4$ PgC/yr for 1990-1999, and without any adjustment for $F_{NAT,NS}$. We compare estimate of $F_{NET} - F_{RIV}$ from LDEO-HPD and other products (Table 5) to these estimates.

360

2.9 Observational-based products

361

362

363

We compare the pCO₂ error statistics and CO₂ flux estimates to four products that extrapolate from SOCAT data to global coverage using machine learning or other statistical modeling techniques (Table 5).

Table 5. Observational data products for comparison to these results

Observation-based pCO ₂ product	Reference
MPI-SOMFFN	Landschützer et al. (2014); Landschützer, Gruber, and Bakker (2020)
JENA-MLS	Rödenbeck et al. (2014)
CMEMS	Denvil-Sommer et al. (2019)
CSIR	Gregor et al. (2019)

3 Results

With LDEO-HPD, an XGB algorithm estimates time-varying maps of model-data misfit, and these misfits are then used to adjust model fields to arrive at an estimate of the real-world pCO₂, from which CO₂ flux is then calculated. By identifying large-scale patterns of model mismatch with observations (section 3.1), LDEO-HPD approach reconstructs real-world pCO₂ with greater fidelity than other recently-published approaches (section 3.2). After correcting for riverine outgassing, air-sea CO₂ flux estimates from LDEO-HPD are consistent with independent observations for both 1990-1999 and 1994-2007 (section 3.3).

3.1 Model-data misfit

The 9-model, global-mean bias of 10 μatm in ocean pCO₂ (Figure 1D) can partially be attributed to neglecting to account for the water vapor correction when calculating the atmospheric pCO₂ that forces the model (Dickson et al., 2007). If the molar concentration of CO₂ is measured in dry air then, by standard protocol (Orr et al., 2017), the atmospheric partial pressure of CO₂ must be reduced by the vapor pressure of water (equation 5):

$$pCO_{2,atm} = xCO_2(P - VP_{H_2O}) \quad (5)$$

where $pCO_{2,atm}$ is the partial pressure of CO₂ in atmosphere, xCO_2 the molar concentration of CO₂ in dry air, P is atmospheric pressure in wet air, and VP_{H_2O} is vapor pressure of water. This is typically a small percentage correction, but still a change in the pressure field of only 3% changes the partial pressure of CO₂ by about 10 μatm . Thus, if the water vapor correction is ignored, the partial pressure of CO₂ in the atmosphere that the ocean model experiences will be too high and ocean pCO₂ will also be high. Of the nine models, three do not account for this correction, and the other six do (Friedlingstein et al., 2020). Hauck et al. (2020) illustrate through comparison to SOCAT data that these models have a significant high bias in pCO₂. In addition, they show that several models that do include the water vapor correction also have a high pCO₂ bias, but do not identify the source of this error. The mean pCO₂ bias of +10 μatm that we find (Figure 1D) is thus partially, but not fully, attributable to several models not applying the water vapor correction.

The model corrections solved for by the XGB algorithm has significant spatial structure, and thus is doing far more than just addressing a global-mean bias in the GOBM priors. This is illustrated for two of the nine models in Figure 4. There are distinct patterns and consistent seasonality in the required corrections. For the MPI model, in the Southern Ocean and North Pacific, pCO₂ is far too high in winter (JJA) and far too low in summer (DJF), thus the XGB algorithm imposes strong negative and positive corrections, respectively. In the North Atlantic, however, winter is too low and summer is too high, requiring the opposite sign of corrections. In the subtropics, MPI requires a strong negative correction. For CNRM, these patterns are different, with the whole of the winter hemisphere generally being slightly too low in pCO₂ and the majority of the summer hemisphere being too high in pCO₂, requiring modest positive and negative cor-

404 rection, respectively. Both models require a positive correction in the equatorial Pacific.
 405 Zonal-average misfits (Figure 4B) indicate that both of these model require the same sign
 406 and comparable magnitude seasonal correction in the extratropical Northern Hemisphere,
 407 while MPI requires much larger corrections in the Southern Ocean.

408 The seasonality of model-data misfits (Figure 4) indicate that the LDEO-HPD is
 409 correcting for errors in model representation of seasonal physical and biogeochemical pro-
 410 cesses, such as mixed layer deepening and biological processes. These machine-learning
 411 derived maps of model-data misfit could be applied as a diagnostic of model performance
 412 to offer a larger-scale perspective that complements direct comparison to in situ data (Hauck
 413 et al., 2020). Model development could be supported with this approach to model-data
 414 comparison.

415 3.2 Evaluation of LDEO-HPD against independent datasets

416 At the ocean timeseries sites at Bermuda (BATS) and Hawaii (HOT), LDEO-HPD
 417 compares quite favorably to the observations. The amplitude of seasonal and interan-
 418 nual variability in LDEO-HPD is as observed at HOT (Figure 5B, 6A) and slightly un-
 419 derestimated at BATS (Figure 5C, 6B), and the trends at both timeseries are well-represented.
 420 Compared to existing pCO₂ gap-filling methods, LDEO-HPD performs slightly better
 421 at BATS and HOT, with the lowest unbiased-RMSE relative to SOMFFN, MLS, and
 422 CMEMS (Figure 6A,B). Correlations are high at HOT and BATS because of the pro-
 423 nounced subtropical seasonality captured in the datasets. All these products are reliably
 424 able to capture subtropical seasonality (Rödenbeck et al., 2015; Gloege et al., 2021; Stamell
 425 et al., 2020).

426 LDEO and GLODAP are global observation datasets from intermittent ship tran-
 427 sects. In these data, seasonality is less well-resolved, a fact that helps to explain the lower
 428 correlations of all products to the data. All the products show similar performance on
 429 LDEO observations, with all the products underestimating the variability (Figure 6C).
 430 For comparison to GLODAP, LDEO-HPD has a smaller unbiased-RMSE relative to other
 431 products (Figure 6D). LDEO-HPD and MLS capture the amplitude of variability in GLO-
 432 DAP equally well, and slightly better than SOMFFN and CMEMS.

433 Over time, the skill of LDEO-HPD against independent observations of LDEO and
 434 GLODAP increases relative to the other methods. In the 1990s, the skill of all methods
 435 are indistinguishable (Figure 7, left). In the 2000s, comparison to GLODAP indicates
 436 that LDEO-HPD is slightly better than the others, though there is no distinction across
 437 the methods for LDEO (Figure 7, center). In the 2010s, LDEO-HPD clearly does the
 438 best job at capturing GLODAP, and is slightly improved against LDEO (Figure 7, right).
 439 Thus, we attribute long-term finding of a better fit to independent observations (Fig-
 440 ure 6) is attributable to the better fit of LDEO-HPD in the later decades (Figure 7).

441 3.3 CO₂ fluxes: 1982-2018

442 Mean pCO₂ and CO₂ flux from LDEO-HPD algorithm for 1982-2018 show well known
 443 features. Elevated pCO₂ is observed at the equator (Figure 8A), especially in the east-
 444 equatorial Pacific. This elevated pCO₂ is the result of upwelling of cold, carbon laden
 445 waters. The surface pCO₂ in this region is greater than the atmosphere, resulting in net
 446 CO₂ flux from the ocean to the atmosphere (Figure 8B).

447 Over time, the net global CO₂ flux has become increasingly negative (Table 6), i.e.
 448 the ocean has become a greater net carbon sink over the recent decades as atmospheric
 449 pCO₂ has risen. Coastal filling (Section 2.6) increases uptake by nearly 0.1 to 0.2 PgC/yr,
 450 consistent with past estimates of globally integrated coastal uptake (Roobaert et al., 2019).

Table 6. Decadal net CO₂ flux (F_{NET}) (PgC/yr)

CO₂ flux from LDEO-HPD across decades without coastal filling (“unfilled”) and filled with the climatology (section 2.6).

	Unfilled	Filled
1982-1990	-1.38	-1.53
1990-2000	-1.48	-1.65
2000-2010	-1.49	-1.69
2010-2018	-1.96	-2.23

451 Applying the same to the calculation of air-sea CO₂ fluxes for all products (Sec-
 452 tion 2.7), and applying the F_{RIV} correction, we find that fluxes estimated by LDEO-HPD
 453 are within the range of the other products for F_{ant} (Figure 9A). Independent flux esti-
 454 mates based on interior data or atmospheric constraints also indicate consistency. Com-
 455 pared to F_{ANT} for 1990-1999 (Denman et al., 2007) and $F_{ANT} + F_{NAT,NS}$ 1994-2007
 456 (Gruber, Clement, et al., 2019), all products are within the uncertainty bounds (Figure
 457 9B).

458 Improved comparison to independent data in LDEO-HPD is consistent with the
 459 reduced skewness of the target variable distribution (Figure 2). Reduced skewness should
 460 particularly improve predictions at the tails of the distribution, which in this case are
 461 the decades of the 1980s and 2010s. We do not have sufficient independent data to make
 462 comparisons in the 1980s, but HPD performs best of all methods in the 2010s (Figure
 463 7, Table 7).

Table 7. RMSE at independent datasets across decades

RMSE in each product against GLODAP and LDEO datasets across three decades: 1990s, 2000s,
 and 2010s. Bold values indicate the product with the lowest RMSE. LDEO values are shown in
 parenthesis.

	1990s	2000s	2010s
LDEO-HPD	22.0 (27.6)	13.8 (19.0)	15.4 (23.4)
SOMFFN	23.3 (28.2)	15.4 (19.9)	16.9 (26.0)
MLS	22.2 (32.7)	16.1 (25.5)	17.7 (31.6)
CMEMS	21.9 (25.8)	16.2 (18.6)	15.9 (24.8)
CSIR	20.8 (28.4)	15.6 (21.2)	15.7 (27.9)

464 4 Discussion

465 We show that incorporating physical models into machine learning algorithms re-
 466 sults in some improvement in predictions of surface ocean pCO₂. Using output from GOBMs
 467 as a prior guess allows us to reduce the skewness of the target variable distribution (Fig-
 468 ure 2). Though GOBMs are imperfect representations of the real ocean (Hauck et al.,
 469 2020), this work illustrates that they can provide useful prior estimates of pCO₂ upon
 470 which data can improve using machine learning algorithms. By merging models and data,

471 LDEO-HPD reduces error in estimates of pCO₂ (Figure 6), with the recent decades be-
 472 ing the most improved (Figure 7, Table 7).

473 The LDEO-HPD approach of correcting GOBMs additionally estimates the mis-
 474 fit between model output and observed pCO₂ at all points in space and time (Figure 3).
 475 These misfit fields offer potential to facilitate model development by highlighting and
 476 visualizing the times and regions where the model performs poorly.

477 LDEO-HPD indicates an ocean carbon sink that is on the upper end of the suite
 478 of products for 1990-1999, but at the lower end of the suite of products for 2009-2018
 479 (Figure 9). This finding is consistent with the reduced skewness in the target variable
 480 in our approach. pCO₂ data the 1980s are extremely sparse, but in the 1990s they are
 481 almost as numerous as in the subsequent decades. The 1980s and 1990s are both skewed
 482 low with respect to the overall pCO₂ distribution due to the long-term increase of sur-
 483 face ocean pCO₂ in response to atmospheric pCO₂ growth. The whole pCO₂ distribu-
 484 tion is centered somewhere between the decades the 1990s and 2000s (Figure 2A,B). Thus,
 485 pCO₂ predictions in since the 2000s in other machine learning approaches are potentially
 486 skewed slightly low, i.e. toward the mean of the overall distribution. A negative bias in
 487 ocean pCO₂ would increase the air-sea pCO₂ difference and drive a greater flux into the
 488 ocean (Equation 2). The opposite direction of skew may be occurring in the 1990s, with
 489 pCO₂ skewed slightly high and fluxes skewed low. Machine learning algorithms are based
 490 on the assumption that the training and testing data are independent and identically
 491 distributed and thus drawn from the same data generating distribution (Goodfellow et
 492 al., 2016). A tighter distribution is easier for a statistical algorithm to fit. By LDEO-
 493 HPD fitting model-data misfit, the skewness of the target variable distribution is largely
 494 eliminated (Figure 2C,D). In comparison to other products, the reduction of skewness
 495 in LDEO-HPD (Figure 2A,B) is consistent with both the improved fit to independent
 496 observations (Figure 7, Table 7), and the slightly larger ocean carbon sink LDEO-HPD
 497 in the 1990s and the slightly smaller sink since 2009 (Figure 9).

498 The combination of data-based machine learning with specific physical constraints
 499 or with the physics embodied in dynamical models is an emerging concept for earth sci-
 500 ence applications (Karpatne et al., 2017; Reichstein et al., 2019). As in other efforts that
 501 have corrected dynamical models using observations (Watt-Meyer et al., 2021), we use
 502 GOBMs as a prior estimate of the surface ocean pCO₂ field, and then correct these fields
 503 with data. The fact that the distribution of the target variable is substantially tightened
 504 (Figure 2A,C) illustrates that GOBMs bring valuable prior physical information to sup-
 505 port a robust reconstruction. For example, where pCO₂ is high, such as in the equato-
 506 rial Pacific, it is also high in the model; and thus model-data misfits are constrained in
 507 magnitude (Figure 2C). If the GOBMs did not provide a useful prior, i.e. had little re-
 508 lationship to the observations, the spread of model-data misfit would be expected to be
 509 larger than of pCO₂ alone. Tightening the distribution of the target variable supports
 510 our improved machine learning based predictions (Figure 6, 7).

511 Gregor et al. (2019) suggest we may have "hit a wall" in our ability to extrapolate
 512 sparse pCO₂ data to global coverage. Here, we illustrate that incorporating model out-
 513 put and addressing skewness of the target variable distribution allows some additional
 514 improvement in prediction skill. In addition, LDEO-HPD employs an XGB algorithm,
 515 which is also found to be promising by Gregor et al. (2019). Stamell et al. (2020) showed
 516 the XGB algorithm performs slightly better in pCO₂ extrapolation than neural network
 517 or random forest algorithms. XGB's strength is its self-correcting nature in which each
 518 additional tree improves upon errors made in the previous.

519 For 2009-2018, the Global Carbon Budget 2020 (Friedlingstein et al., 2020) indi-
 520 cates an ocean anthropogenic sink (F_{ANT}) of -2.5 ± 0.6 PgC/yr (Figure 9). LDEO-HPD
 521 indicates a similar flux, -2.6 ± 0.28 PgC/yr ($F_{ANT} = F_{NET} - F_{RIV}$). The standard de-
 522 viation across the nine error-corrected GOBMs (0.1 PgC/yr) and the uncertainty asso-

523 ciated with F_{RIV} (0.26 PgC/yr) are added in quadrature to produce the total uncertainty
 524 of LDEO-HPD. The other four products discussed here (Table 5) have mean uptake of
 525 -2.6 ± 0.26 to -2.8 ± 0.26 PgC/yr, using $F_{RIV} = +0.49 \pm 0.26$ PgC/yr to calculate F_{ANT}
 526 from F_{NET} for all. Thus, all products are consistent with the GCB2020. It is important
 527 to note that our updated estimate of F_{RIV} is lower than that used by the Global Car-
 528 bon Budget 2020 (+0.61 PgC/yr), and by Hauck et al. (2020) (+0.78 PgC/yr), thus re-
 529 ducing the apparent model to observation product discrepancy that has been previously
 530 discussed (Friedlingstein et al., 2020). In addition, the harmonized flux calculation ap-
 531 proach used here slightly reduces ocean uptake for some products (Fay et al., 2021). In
 532 summary, for 2009-2018, we find that all products fall within the uncertainties of the GCB2020
 533 for F_{ANT} , with LDEO-HPD on the lower end of the range and slightly closer to the GCB2020
 534 mean.

535 5 Conclusions

536 To reconstruct the real ocean’s surface ocean pCO_2 , LDEO-HPD rectifies output
 537 of nine global ocean biogeochemical models (GOBMs) by learning the misfit from ob-
 538 served pCO_2 using an XGB algorithm and observed driver fields. LDEO-HPD improves
 539 prediction accuracy compared to other state-of-the-art pCO_2 data products, as indicated
 540 by improved fit to independent data. This suggests that GOBM output adds useful prior
 541 information to machine learning for this application. The globally and temporally com-
 542 plete misfits learned by the algorithm additionally have promise as a new diagnostic and
 543 visualization tool with which GOBM performance can be assessed. Adding physical in-
 544 formation, here by using GOBMs as a prior, and addressing temporal skewness in sur-
 545 face ocean pCO_2 distribution offer promising directions for continued improvement in
 546 the fidelity of machine-learning based reconstructions of the ocean carbon sink. The LDEO-
 547 HPD suggests a global ocean sink for anthropogenic carbon that is within the range of
 548 the suite of existing pCO_2 observation-based products, and that is in agreement with
 549 the Global Carbon Budget 2020 (Friedlingstein et al., 2020).

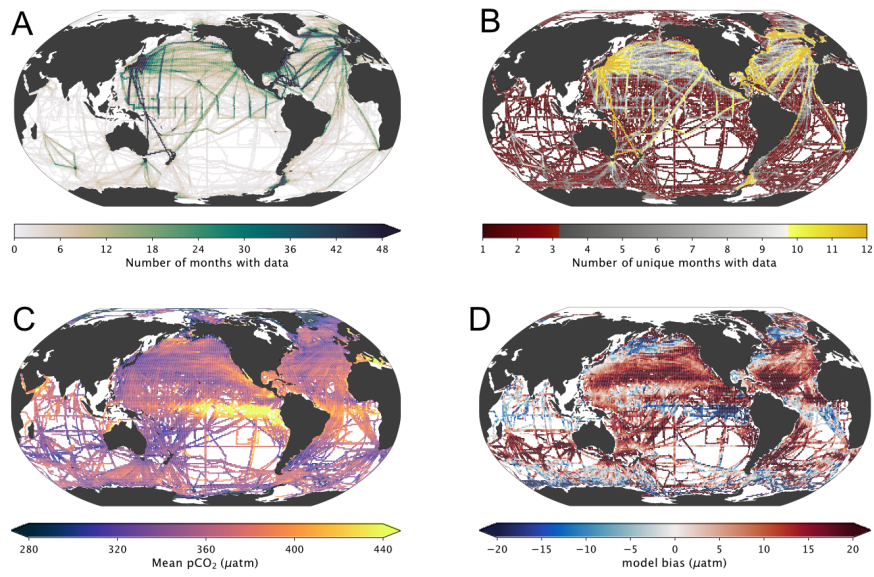


Figure 1. A) Total number of months over 1982-2018 with observations. B) Number of unique months with observations. C) Long-term mean pCO₂ at each 1°x1° pixel. D) Bias between SOCAT and mean of nine GOBMs.

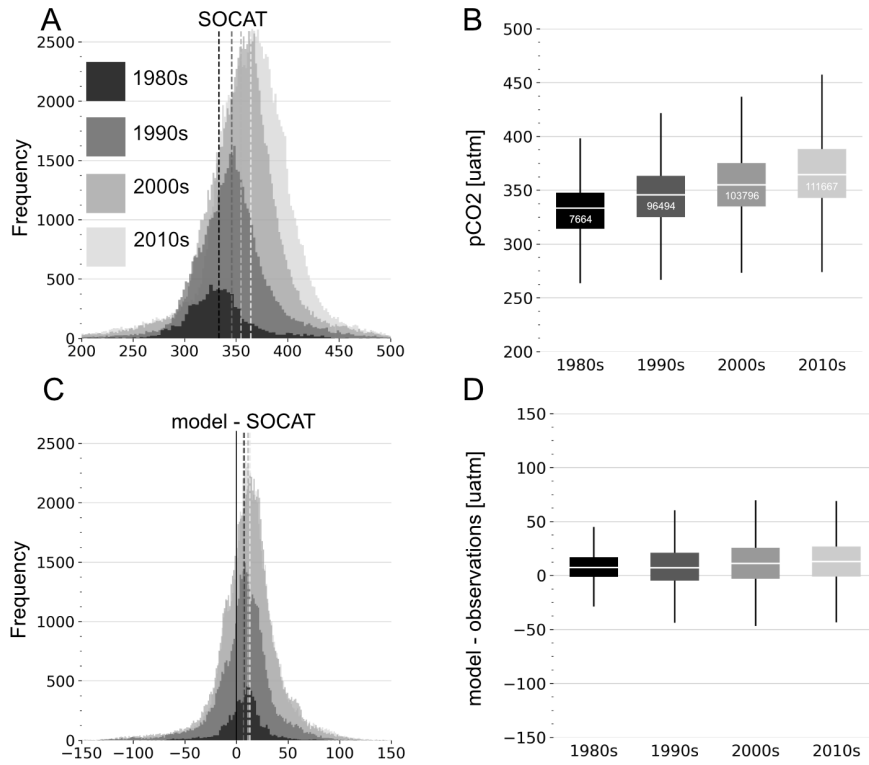


Figure 2. A) Histogram of SOCAT pCO₂ observations in 1980s, 1990s, 2000s and 2010s shown by different shades of gray. Dotted line indicates mean pCO₂. B) boxplot of observations for each decade. Whisker indicates 1.5*IQR, observations outside the whisker have been omitted. White line indicates the mean and the number inside in the box indicates the number of observations within that decade. C) Histogram of the difference between CEM3 model and SOCAT and D) is the corresponding boxplot. Due to different internal model structures, the long-term trend from 1980s to 2010s varies from -7 µatm to +9 µatm.

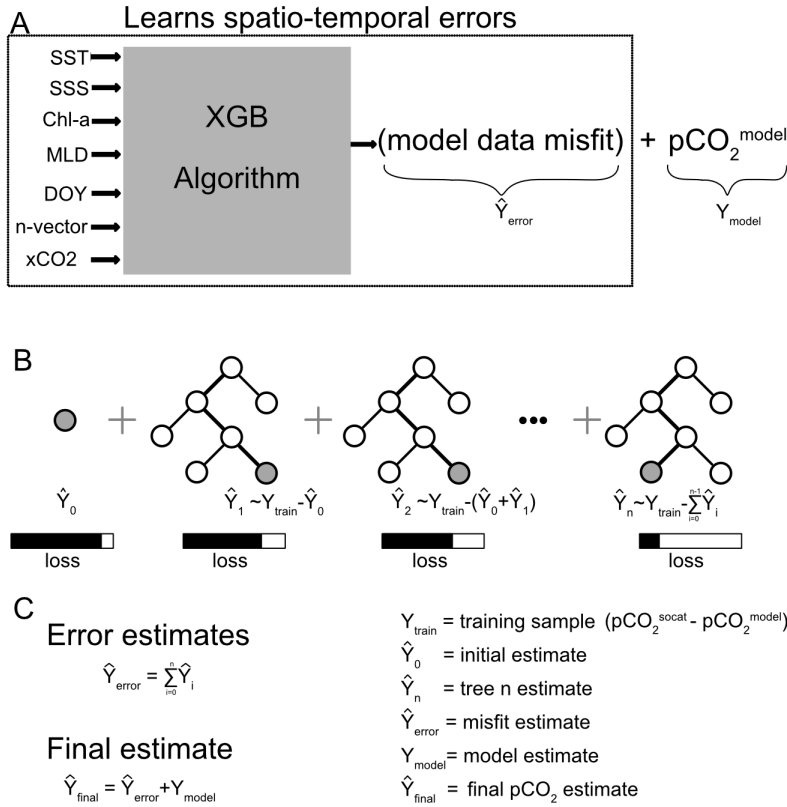


Figure 3. A) Schematic of LDEO-HPD method. A relationship between a suite of auxiliary features and the model data misfit is learned via the XGB algorithm. Spatio-temporal errors are then added back to the model’s pCO₂ field to create the final product. B) outlines the XGB algorithm, where decision trees are sequentially added to improve the mistakes of the previous trees. Each additional tree reduces the loss and improves the overall performance of the algorithm. C) The final estimate of pCO₂ is the model-data misfit estimated at all global points plus the original model. This process is done independently for each of the 9 GOBMs and the final estimate is the average pCO₂.

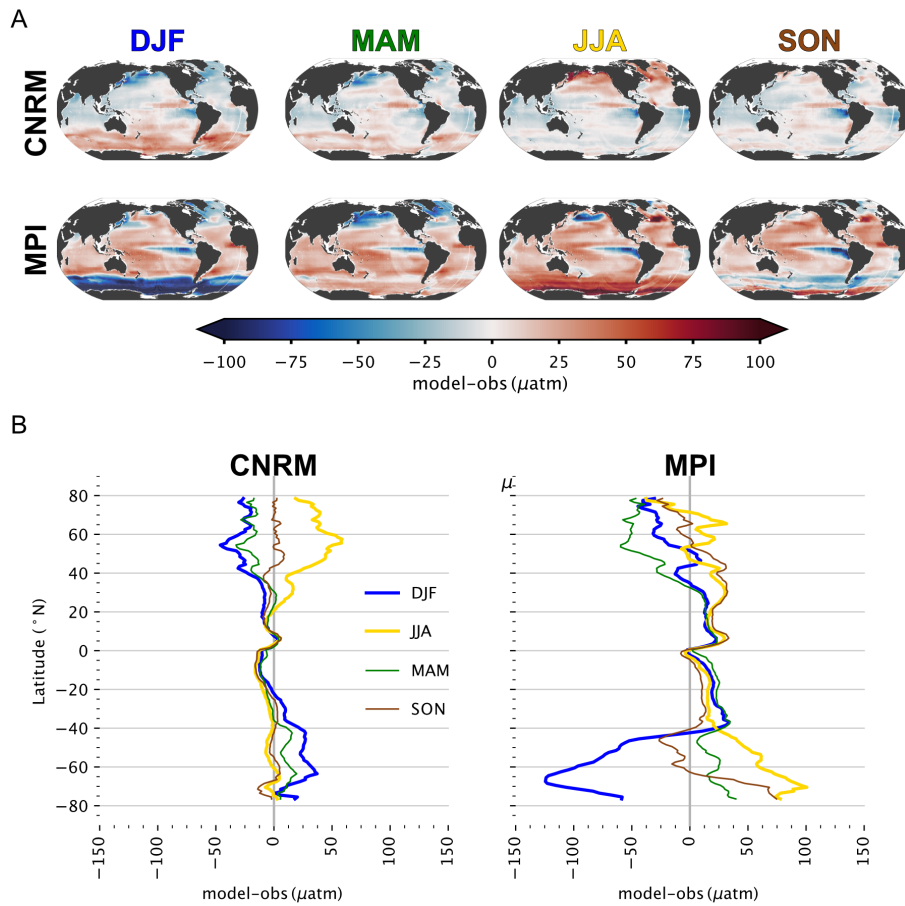


Figure 4. A) Average pCO₂ misfit in the MPI and CNRM model for all years, December, January, and February (DJF); March, April and May (MAM); June, July, and August (JJA); and September October and November (SON). B) Zonally average pCO₂ misfit in the MPI and CNRM models for DJF, JJA, MAM, and SON.

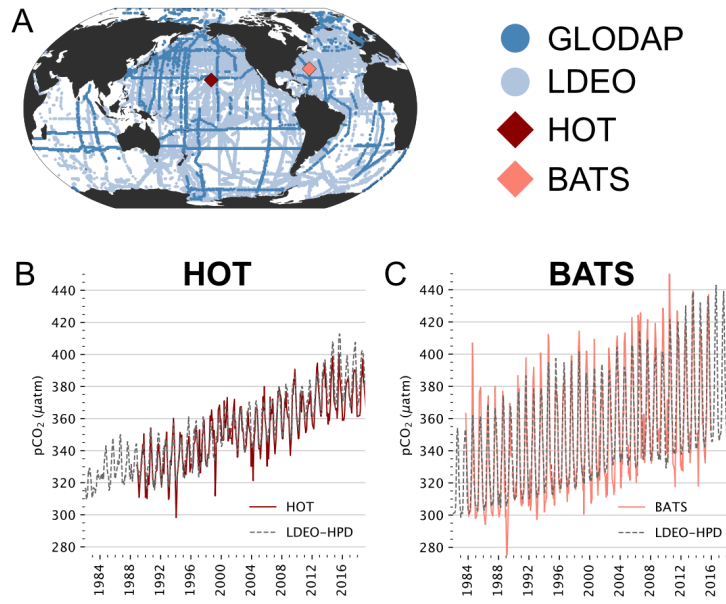


Figure 5. A) Locations of independent datasets. BATS and HOT are timeseries, while the GLODAP and LDEO are spatially varying. B) comparison of HOT with LDEO-HPD output. C) comparison between BATS and LDEO-HPD output

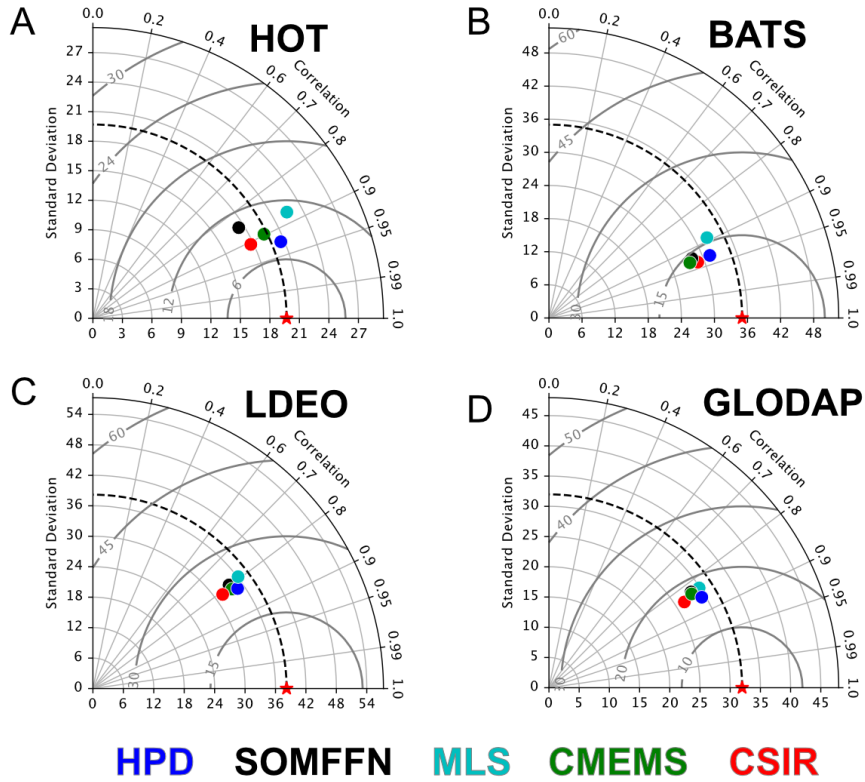


Figure 6. Taylor diagrams display the performance of published gap-filling techniques and LDEO-HPD product. Performance is evaluated at two timeseries: A) HOT and B) BATS; and two global datasets: C) LDEO and D) GLODAP. Red star indicates standard deviation of each dataset.

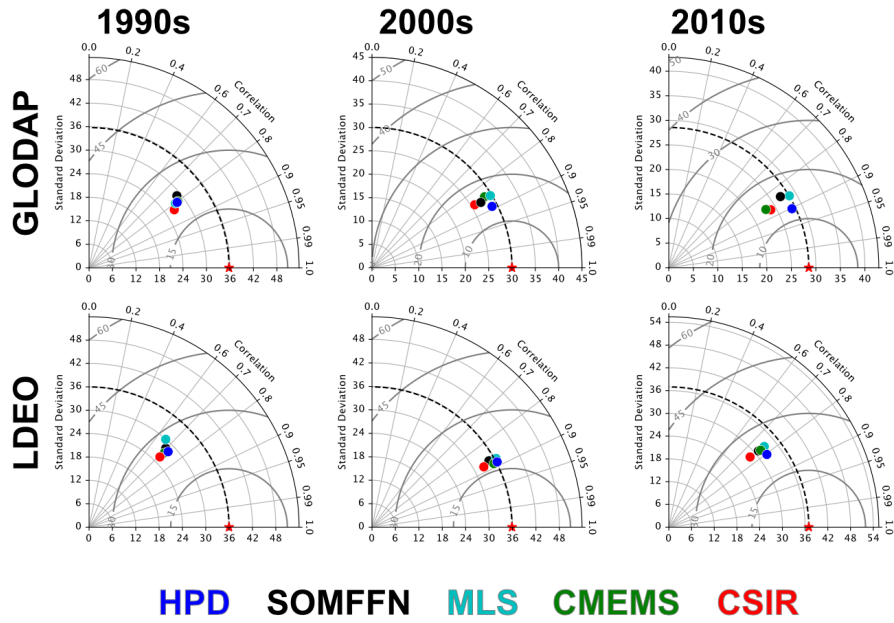


Figure 7. Taylor diagrams display the performance of published gap-filling techniques and LDEO-HPD product. Performance is evaluated at two global datasets, LDEO and GLODAP, using data in the from 1990-1999 (1990s), 2000-2009 (2000s), and 2010-2018 (2010s). Red star indicates standard deviation of each dataset.

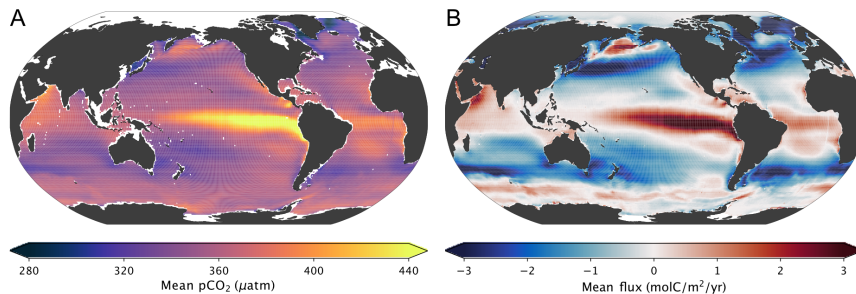


Figure 8. Mean A) pCO₂ and B) net CO₂ flux over 1982-2018 estimated from LDEO-HPD. A spatially complete map of CO₂ flux is achieved by filling in gaps with a trend plus climatology.

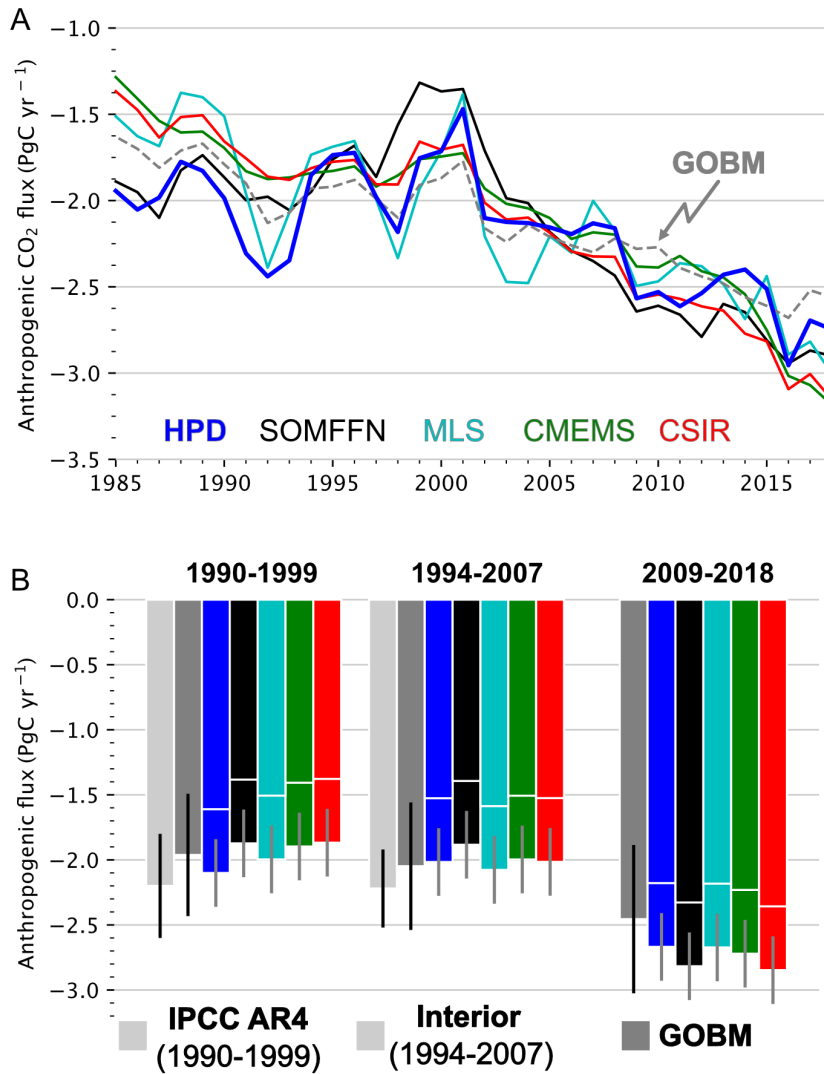


Figure 9. A) Anthropogenic air-sea CO_2 exchange (F_{ANT}) for 1985-2018 from LDEO-HPD and four other products: SOMFFN, MLS, CMEMS, CSIR-ML6. Positive is to the atmosphere. Gray dash is the mean of the 9 GOBM priors, which are also the basis for the ocean sink estimate of the Global Carbon Budget 2020 (Friedlingstein et al., 2020). B) Anthropogenic CO_2 flux for 1990-99, 1994-2007, and 2009-2018. Light gray bar indicates IPCC AR4 or interior observation-based estimates with uncertainty. Dark gray bar is the mean of the nine GOBMs. Colored bars indicate observation-based estimates. The white line separates F_{NET} from the products and F_{RIV} , estimated as the average of three estimates (0.49 PgC/yr), see section 2.8

550 **Acknowledgments**

551 We acknowledge support from Columbia University. M.Y acknowledges support from the
 552 Data Science Institute scholar program. The Surface Ocean CO_2 Atlas (SOCAT) is an
 553 international effort, endorsed by the International Ocean Carbon Coordination Project
 554 (IOCCP), the Surface Ocean Lower Atmosphere Study (SOLAS) and the Integrated Marine
 555 Biosphere Research (IMBeR) program, to deliver a uniformly quality-controlled sur-
 556 face ocean CO_2 database. The many researchers and funding agencies responsible for

557 the collection of data and quality control are thanked for their contributions to SOCAT.
 558 We acknowledge data were collected and made freely available by the Southern Ocean
 559 Carbon and Climate Observations and Modeling (SOCCOM) Project funded by the Na-
 560 tional Science Foundation, Division of Polar Programs (NSF PLR -1425989), supplemented
 561 by NASA, and by the International Argo Program and the NOAA programs that con-
 562 tribute to it. (<http://www.argo.ucsd.edu>, <http://argo.jcommops.org>). The Argo Pro-
 563 gram is part of the Global Ocean Observing System. Analysis scripts and LDEO-HPD
 564 code is available at <https://github.com/lglloege/LDEO-HPD> and LDEO-HPD output
 565 is available at <https://zenodo.org/record/4760205>.

566 References

- 567 Adcroft, A., Anderson, W., Balaji, V., Blanton, C., Bushuk, M., Dufour, C. O., ...
 568 others (2019). The gfdl global ocean and sea ice model om4. 0: Model descrip-
 569 tion and simulation features. *Journal of Advances in Modeling Earth Systems*,
 570 *11*(10), 3167–3211.
- 571 Aumont, O., Éthé, C., Tagliabue, A., Bopp, L., & Gehlen, M. (2015). Pisces-v2:
 572 an ocean biogeochemical model for carbon and ecosystem studies. *Geoscientific*
 573 *Model Development Discussions*, *8*(2).
- 574 Aumont, O., Orr, J. C., Monfray, P., Ludwig, W., Amiotte Suchet, P., & Probst,
 575 J. L. (2001, June). Riverine-driven interhemispheric transport of carbon.
 576 *Global Biogeochem. ...*, *15*, 393–405.
- 577 Bakker, D. C. E., Pfeil, B., Landa, C. S., Metzl, N., O’Brien, K. M., Olsen, A., ...
 578 Xu, S. (2016). A multi-decade record of high-quality f_{CO_2} data in version 3 of
 579 the surface ocean CO_2 atlas (socat). *Earth System Science Data*, *8*(2), 383–413.
 580 Retrieved from <https://www.earth-syst-sci-data.net/8/383/2016/> doi:
 581 10.5194/essd-8-383-2016
- 582 Bates, N. R. (2007). Interannual variability of the oceanic CO_2 sink in the subtropical
 583 gyre of the north atlantic ocean over the last 2 decades. *Journal of Geophysical*
 584 *Research: Oceans*, *112*(C9).
- 585 Berthet, S., Séférian, R., Bricaud, C., Chevallier, M., Voldoire, A., & Ethé, C.
 586 (2019). Evaluation of an online grid-coarsening algorithm in a global eddy-
 587 admitting ocean biogeochemical model. *Journal of Advances in Modeling Earth*
 588 *Systems*, *11*(6), 1759–1783.
- 589 Bockmon, E. E., & Dickson, A. G. (2015). An inter-laboratory comparison assessing
 590 the quality of seawater carbon dioxide measurements. *Marine Chemistry*, *171*,
 591 36–43.
- 592 Buitenhuis, E. T., Hashioka, T., & Quéré, C. L. (2013). Combined constraints on
 593 global ocean primary production using observations and models. *Global Bio-*
 594 *geochemical Cycles*, *27*(3), 847–858.
- 595 Chen, T., & Guestrin, C. (2016). Xgboost: A scalable tree boosting system. In
 596 *Proceedings of the 22nd acm sigkdd international conference on knowledge*
 597 *discovery and data mining* (pp. 785–794).
- 598 Denman, K. L., Brasseur, G. P., Chidthaisong, A., Ciais, P., Cox, P. M., Dickinson,
 599 R. E., ... Steffen, W. (2007). Couplings between changes in the climate sys-
 600 tem and biogeochemistry. In *Climate change 2007: The physical science basis*
 601 (p. 499-588). United States: Cambridge University Press.
- 602 Denvil-Sommer, A., Gehlen, M., Vrac, M., & Mejia, C. (2019). Lsce-fnn-v1: a
 603 two-step neural network model for the reconstruction of surface ocean pCO_2
 604 over the global ocean. *Geoscientific Model Development*, *12*(5), 2091–2105.
 605 Retrieved from <https://www.geosci-model-dev.net/12/2091/2019/> doi:
 606 10.5194/gmd-12-2091-2019
- 607 Dickson, A. G., Sabine, C. L., & Christian, J. R. (2007). *Guide to best practices for*
 608 *ocean CO_2 measurements*. North Pacific Marine Science Organization.
- 609 Doney, S. C., Lima, I., Feely, R. A., Glover, D. M., Lindsay, K., Mahowald, N., ...

- 610 Wanninkhof, R. (2009). Mechanisms governing interannual variability in
 611 upper-ocean inorganic carbon system and air–sea CO₂ fluxes: Physical climate
 612 and atmospheric dust. *Deep Sea Research Part II: Topical Studies in Oceanog-*
 613 *raphy*, *56*(8-10), 640–655.
- 614 Dore, J. E., Lukas, R., Sadler, D. W., Church, M. J., & Karl, D. M. (2009). Physical
 615 and biogeochemical modulation of ocean acidification in the central north pa-
 616 cific. *Proceedings of the National Academy of Sciences*, *106*(30), 12235–12240.
- 617 Fay, A., Gregor, L., Landschützer, P., McKinley, G. A., Gruber, N., Gehlen, M.,
 618 ... Zeng, J. (2021). Harmonization of global surface ocean pCO₂ mapped
 619 products and their flux calculations; an improved estimate of the ocean carbon
 620 sink. *Earth System Science Data*, *submitted*.
- 621 Friedlingstein, P., Jones, M. W., O’Sullivan, M., Andrew, R. M., Hauck, J., Peters,
 622 G. P., ... Zaehle, S. (2019). Global Carbon Budget 2019. *Earth System*
 623 *Science Data*, *11*(4), 1783–1838.
- 624 Friedlingstein, P., O’Sullivan, M., Jones, M. W., Andrew, R. M., Hauck, J., Olsen,
 625 A., ... others (2020). Global carbon budget 2020. *Earth System Science Data*,
 626 *12*(4), 3269–3340.
- 627 Gade, K. (2010). A non-singular horizontal position representation. *The journal of*
 628 *navigation*, *63*(3), 395–417.
- 629 Gloege, L., McKinley, G., Landschützer, P., Fay, A., Frölicher, T., Fyfe, J., ... oth-
 630 ers (2021). Quantifying errors in observationally-based estimates of ocean
 631 carbon sink variability. *GBC (in press)*.
- 632 Goodfellow, I., Bengio, Y., & Courville, A. (2016). *Deep learning*. MIT Press.
 633 (<http://www.deeplearningbook.org>)
- 634 Gregor, L., & Gruber, N. (2021, March). OceanSODA-ETHZ: a global grid-
 635 ded data set of the surface ocean carbonate system for seasonal to decadal
 636 studies of ocean acidification. *Earth System Science Data*, 1–32. doi:
 637 10.5194/essd-13-777-2021
- 638 Gregor, L., Kok, S., & Monteiro, P. (2017). Empirical methods for the estimation
 639 of southern ocean CO₂: support vector and random forest regression. *Biogeo-*
 640 *sciences*, *14*(23), 5551–5569.
- 641 Gregor, L., Lebehof, A. D., Kok, S., & Scheel Monteiro, P. M. (2019). A compar-
 642 ative assessment of the uncertainties of global surface ocean CO₂ estimates
 643 using a machine-learning ensemble (CSIR-ML6 version 2019a)—have we hit the
 644 wall? *Geoscientific Model Development*, *12*(12), 5113–5136.
- 645 Gruber, N., Clement, D., Carter, B. R., Feely, R. A., Van Heuven, S., Hoppema, M.,
 646 ... Wanninkhof, R. (2019, March). The oceanic sink for anthropogenic CO₂
 647 from 1994 to 2007. *Science*, *363*(6432), 1193–1199.
- 648 Gruber, N., Landschützer, P., & Lovenduski, N. S. (2019). The variable Southern
 649 Ocean carbon sink. *Annual Review of Marine Science*, *11*, 159–186.
- 650 Hain, M. P., Sigman, D. M., Higgins, J. A., & Haug, G. H. (2015). The effects of
 651 secular calcium and magnesium concentration changes on the thermodynam-
 652 ics of seawater acid/base chemistry: Implications for eocene and cretaceous
 653 ocean carbon chemistry and buffering. *Global Biogeochemical Cycles*, *29*(5),
 654 517–533.
- 655 Harada, Y., Kamahori, H., Kobayashi, C., Endo, H., Kobayashi, S., Ota, Y., ...
 656 Takahashi, K. (2016). The jra-55 reanalysis: Representation of atmospheric
 657 circulation and climate variability. *Journal of the Meteorological Society of*
 658 *Japan. Ser. II*, *94*(3), 269–302.
- 659 Hauck, J., Zeising, M., Le Quéré, C., Gruber, N., Bakker, D. C. E., Bopp, L., ...
 660 Séférian, R. (2020, October). Consistency and challenges in the ocean carbon
 661 sink estimate for the Global Carbon Budget. *Frontiers in Marine Science*, *7*,
 662 3167.
- 663 Hersbach, H., Bell, B., Berrisford, P., Hirahara, S., Horányi, A., Muñoz-Sabater, J.,
 664 ... others (2020). The era5 global reanalysis. *Quarterly Journal of the Royal*

- 665 *Meteorological Society*, 146(730), 1999–2049.
- 666 Jacobson, A. R., Mikaloff Fletcher, S. E., Gruber, N., Sarmiento, J. L., & Gloor, M.
667 (2007, March). A joint atmosphere-ocean inversion for surface fluxes of carbon
668 dioxide: 1. Methods and global-scale fluxes. *Global Biogeochemical Cycles*,
669 21(1), 273.
- 670 Karpatne, A., Watkins, W., Read, J., & Kumar, V. (2017). Physics-guided neural
671 networks (pgnn): An application in lake temperature modeling. *arXiv preprint*
672 *arXiv:1710.11431*.
- 673 Lacroix, F., Ilyina, T., & Hartmann, J. (2020). Oceanic co₂ outgassing and biolog-
674 ical production hotspots induced by pre-industrial river loads of nutrients and
675 carbon in a global modeling approach. *Biogeosciences*, 17(1), 55–88.
- 676 Landschützer, P., Gruber, N., Bakker, D., & Schuster, U. (2014). Recent variabil-
677 ity of the global ocean carbon sink. *Global Biogeochemical Cycles*, 28(9), 927–
678 949.
- 679 Landschützer, P., Gruber, N., & Bakker, D. C. (2016). Decadal variations and
680 trends of the global ocean carbon sink. *Global Biogeochemical Cycles*, 30(10),
681 1396–1417.
- 682 Landschützer, P., Gruber, N., & Bakker, D. C. (2020). *An observation-based global*
683 *monthly gridded sea surface pco₂ product from 1982 onward and its monthly*
684 *climatology (ncei accession 0160558). version 5.5. noaa national centers for*
685 *environmental information*. Retrieved from [https://www.ncei.noaa.gov/](https://www.ncei.noaa.gov/access/ocean-carbon-data-system/oceans/SPC02_1982_present_ETH_SOM_FFN.html)
686 [access/ocean-carbon-data-system/oceans/SPC02_1982_present_ETH_SOM](https://www.ncei.noaa.gov/access/ocean-carbon-data-system/oceans/SPC02_1982_present_ETH_SOM_FFN.html)
687 [_FFN.html](https://www.ncei.noaa.gov/access/ocean-carbon-data-system/oceans/SPC02_1982_present_ETH_SOM_FFN.html) doi: doi.org/10.7289/V5Z899N6
- 688 Landschützer, P., Laruelle, G. G., Roobaert, A., & Regnier, P. (2020, May). A uni-
689 form pCO₂ climatology combining open and coastal oceans. *Earth System Sci-*
690 *ence Data*, 1–30.
- 691 Law, R. M., Ziehn, T., Matear, R. J., Lenton, A., Chamberlain, M. A., Stevens,
692 L. E., ... others (2017). The carbon cycle in the australian community cli-
693 mate and earth system simulator (access-esm1)–part 1: Model description and
694 pre-industrial simulation. *Geoscientific Model Development*, 10(7), 2567.
- 695 Le Quéré, C., Raupach, M. R., Canadell, J. G., Marland, G., Bopp, L., Ciais, P.,
696 ... others (2009). Trends in the sources and sinks of carbon dioxide. *Nature*
697 *geoscience*, 2(12), 831–836.
- 698 Lueker, T. J., Dickson, A. G., & Keeling, C. D. (2000). Ocean pco₂ calculated from
699 dissolved inorganic carbon, alkalinity, and equations for k₁ and k₂: validation
700 based on laboratory measurements of co₂ in gas and seawater at equilibrium.
701 *Marine chemistry*, 70(1-3), 105–119.
- 702 McKinley, G. A., Fay, A. R., Eddebbbar, Y. A., Gloege, L., & Lovenduski, N. S.
703 (2020, June). External Forcing Explains Recent Decadal Variability of the
704 Ocean Carbon Sink. *AGU Advances*, 1(2), 1.
- 705 McKinley, G. A., Pilcher, D. J., Fay, A. R., Lindsay, K., Long, M. C., & Lovenduski,
706 N. S. (2016, February). Timescales for detection of trends in the ocean carbon
707 sink. *Nature*, 530(7591), 469–472.
- 708 Mears, C. A., Scott, J., Wentz, F. J., Ricciardulli, L., Leidner, S. M., Hoffman, R., &
709 Atlas, R. (2019). A near-real-time version of the cross-calibrated multiplatform
710 (ccmp) ocean surface wind velocity data set. *Journal of Geophysical Research:*
711 *Oceans*, 124(10), 6997–7010.
- 712 Orr, J. C., Najjar, R. G., Aumont, O., Bopp, L., Bullister, J. L., Danabasoglu, G.,
713 ... others (2017). Biogeochemical protocols and diagnostics for the cmip6
714 ocean model intercomparison project (omip). *Geoscientific Model Develop-*
715 *ment*, 10(6), 2169–2199.
- 716 Paulsen, H., Ilyina, T., Six, K. D., & Stemmler, I. (2017). Incorporating a prognostic
717 representation of marine nitrogen fixers into the global ocean biogeochemical
718 model hamocc. *Journal of Advances in Modeling Earth Systems*, 9(1), 438–
719 464.

- 720 Peters, G. P., Le Quéré, C., Andrew, R. M., Canadell, J. G., Friedlingstein, P., Ily-
721 ina, T., . . . Tans, P. (2017). Towards real-time verification of CO₂ emissions.
722 *Nature Climate Change*, *7*(12), 848–850.
- 723 Raupach, M. R., Gloor, M., Sarmiento, J. L., Canadell, J. G., Frolicher, T. L.,
724 Gasser, T., . . . Trudinger, C. M. (2014). The declining uptake rate of at-
725 mospheric CO₂ by land and ocean sinks. *Biogeosciences*, *11*(13), 3453–3475.
- 726 Reichstein, M., Camps-Valls, G., Stevens, B., Jung, M., Denzler, J., Carvalhais, N.,
727 et al. (2019). Deep learning and process understanding for data-driven earth
728 system science. *Nature*, *566*(7743), 195.
- 729 Resplandy, L., Keeling, R., Rödenbeck, C., Stephens, B., Khatiwala, S., Rodgers, K.,
730 . . . Tans, P. (2018). Revision of global carbon fluxes based on a reassessment
731 of oceanic and riverine carbon transport. *Nature Geoscience*, *11*(7), 504–509.
- 732 Ridge, S., & McKinley, G. A. (2020). Ocean carbon uptake under aggressive emis-
733 sion mitigation. *Biogeosciences Discussions*. doi: 10.5194/bg-2020-254
- 734 Rödenbeck, C., Bakker, D., Metzl, N., Olsen, A., Sabine, C., Cassar, N., . . .
735 Heimann, M. (2014). Interannual sea–air co₂ flux variability from an
736 observation-driven ocean mixed-layer scheme. *Biogeosciences*, *11*(17), 4599–
737 4613.
- 738 Rödenbeck, C., Bakker, D. C., Gruber, N., Iida, Y., Jacobson, A. R., Jones, S., . . .
739 others (2015). Data-based estimates of the ocean carbon sink variability—first
740 results of the surface ocean pco₂ mapping intercomparison (socom). *Biogeo-*
741 *sciences*, *12*, 7251–7278.
- 742 Roobaert, A., Laruelle, G. G., Landschützer, P., Gruber, N., Chou, L., & Regnier,
743 P. (2019, December). The Spatiotemporal Dynamics of the Sources and Sinks
744 of CO₂ in the Global Coastal Ocean. *Global Biogeochemical Cycles*, *33*(12),
745 1693–1714. doi: 10.1016/j.polar.2016.03.006
- 746 Sabine, C. L., Hankin, S., Koyuk, H., Bakker, D. C. E., Pfeil, B., Olsen, A.,
747 . . . Yoshikawa-Inoue, H. (2013). Surface ocean co₂ atlas (socat) grid-
748 ded data products. *Earth System Science Data*, *5*(1), 145–153. Re-
749 trieved from <https://www.earth-syst-sci-data.net/5/145/2013/> doi:
750 10.5194/essd-5-145-2013
- 751 Sasse, T., McNeil, B., & Abramowitz, G. (2013). A novel method for diagnosing
752 seasonal to inter-annual surface ocean carbon dynamics from bottle data using
753 neural networks. *Biogeosciences*, *10*(6), 4319–4340.
- 754 Schwinger, J., Goris, N., Tjiputra, J. F., Kriest, I., Bentsen, M., Bethke, I., . . .
755 Heinze, C. (2016). Evaluation of noesm-oc (versions 1 and 1.2), the ocean
756 carbon-cycle stand-alone configuration of the norwegian earth system model
757 (noesm1). *Geoscientific Model Development*, *9*, 2589–2622.
- 758 Stamell, J., Rustagi, R. R., Gloege, L., & McKinley, G. A. (2020). Strengths and
759 weaknesses of three machine learning methods for pco₂ interpolation. *Geosci-*
760 *entific Model Development Discussions*, 1–25.
- 761 Stow, C. A., Jolliff, J., McGillicuddy Jr, D. J., Doney, S. C., Allen, J. I., Friedrichs,
762 M. A., . . . Wallhead, P. (2009). Skill assessment for coupled biological/physical
763 models of marine systems. *Journal of Marine Systems*, *76*(1-2), 4–15.
- 764 Takahashi, T., Sutherland, S. C., & Kozyr, A. (2019). Global ocean surface water
765 partial pressure of co₂ database: measurments performed during 1957–2018
766 (version 2018).
- 767 Taylor, K. E. (2001). Summarizing multiple aspects of model performance in a single
768 diagram. *Journal of Geophysical Research: Atmospheres*, *106*(D7), 7183–7192.
- 769 Tjiputra, J. F., Olsen, A., Bopp, L., Lenton, A., Pfeil, B., Roy, T., . . . Heinze, C.
770 (2014). Long-term surface pco₂ trends from observations and models. *Tellus*
771 *B: Chemical and Physical Meteorology*, *66*(1), 23083.
- 772 Wanninkhof, R. (1992). Relationship between wind speed and gas exchange over the
773 ocean. *Journal of Geophysical Research: Oceans*, *97*(C5), 7373–7382.
- 774 Wanninkhof, R. (2014). Relationship between wind speed and gas exchange over the

- 775 ocean revisited. *Limnology and Oceanography: Methods*, 12(6), 351–362.
- 776 Watson, A. J., Schuster, U., Shutler, J. D., Holding, T., Ashton, I. G. C., Land-
777 schützer, P., . . . Goddijn-Murphy, L. (2020, August). Revised estimates of
778 ocean-atmosphere CO₂ flux are consistent with ocean carbon inventory. *Nature*
779 *Communications*, 1–6.
- 780 Watt-Meyer, O., Brenowitz, N., Clark, S. K., Henn, B., Kwa, A., McGibbon,
781 J., . . . Bretherton, C. (2021, January). Correcting weather and climate
782 models by machine learning nudged historical simulations. , 1–13. doi:
783 10.1002/essoar.10505959.1
- 784 Weiss, R. (1974). Carbon dioxide in water and seawater: the solubility of a non-ideal
785 gas. *Marine chemistry*, 2(3), 203–215.